Supporting Information

Boekelheide et al. 10.1073/pnas.1106397108

SI Materials and Methods

Potential Energy Surface. The potential energy surface for the hydride transfer reaction in dihydrofolate reductase (DHFR) is described using the empirical valence bond (EVB) method (1, 2),

$$U(\mathbf{x}^{(j)}) = \frac{1}{2}(V_{\mathrm{r}}(\mathbf{x}^{(j)}) + V_{\mathrm{p}}(\mathbf{x}^{(j)})) - \frac{1}{2}\sqrt{(V_{\mathrm{r}}(\mathbf{x}^{(j)}) - V_{\mathrm{p}}(\mathbf{x}^{(j)}))^2 + 4V_{12}^2}. \qquad \textbf{[S1]}$$

As in the main text, the notation $\mathbf{x}^{(j)} \equiv (\mathbf{q}_j, \mathbf{Q}_1, \ldots, \mathbf{Q}_N)$ is used to indicate the position of ring-polymer bead j and the full set of classical nuclei. The terms $V_{\mathrm{r}}(\mathbf{x}^{(j)})$ and $V_{\mathrm{p}}(\mathbf{x}^{(j)})$ are the molecular mechanics potential energy functions for the system with the hydride covalently bonded to the donor and acceptor atoms, respectively. The constant $V_{12} = 30.6$ kcal/mol is fit to the experimental rate for the intrinsic reaction (3), and the product state potential $V_{\mathrm{p}}(\mathbf{x}^{(j)})$ includes a constant shift of $\Delta_{12} = +101.9$ kcal/mol to match the experimental driving force for the intrinsic reaction (3). The difference in the value for Δ_{12} used here versus in ref. 1 is due to different treatments of the atom-exclusions in the calculation of long-range electrostatic contributions.

Calculation of $V_{\mathrm{r}}(\mathbf{x}^{(j)})$ and $V_{\mathrm{p}}(\mathbf{x}^{(j)})$ is performed using a modified version of the GROMOS 43A1 united atom forcefield (4). These modifications, which again follow previous work (1, 5), are described in Fig. S7. A cutoff distance of 15 Å is applied to short-ranged nonbonding interactions, and electrostatic interactions beyond 9 Å are calculated using the particle mesh Ewald technique (6). The bond-lengths for all nontransferring hydrogen atoms in the system are constrained using the SHAKE algorithm (7).

To avoid sampling configurations of the enzyme that are not relevant to the intrinsic reaction, weak harmonic restraints were introduced between the simulated enzyme and the reference crystal structure (8). To avoid substrate dissociation during the long equilibrium sampling trajectories, weak harmonic restraints ($k = 0.15$ kcal mol^{-1} A^{-2}) are applied to the heavy atoms in the glutamate moiety of the substrate and to the α-carbons of the neighboring α-helix segment composed of residues 26 to 35; to prevent large-scale conformation rearrangements in DHFR (9), weak harmonic restraints ($k = 0.001$ kcal mol^{-1} A^{-2}) are applied to all other heavy atoms in the enzyme. Fig. S8 demonstrates that these restraints do not measurably affect the reactive trajectories used in our analysis of dynamical correlations.

Calculation Details. We initialize and equilibrate the system using the protocol described in ref. 1. The system is initialized from the DHFR crystal structure in the active configuration [Protein Data Bank (PDB) code 1RX2] (8). Crystallographic 2-mercaptoethanol and manganese ions are removed; crystallographic waters are not. The amine side chain of Q102 is rotated 180° to correctly coordinate the adenine moiety of the cofactor (10). To be consistent with the observed hydrogen bonding networks in the crystal structure, histidine residues 45, 124, and 149 are protonated at nitrogen ND1, histidine residues 114 and 141 are protonated at nitrogen NE2, and both DHFR cysteine residues are in their protonated form (11). The enzyme is explicitly solvated using 4,122 SPC/E rigid water molecules (11) in a truncated octahedral simulation cell with constant volume and periodic boundary conditions. The periodic image distance for the cell is 57.686 Å. Twelve Na^+ ions are included for charge neutrality. The full system includes $N = 14{,}080$ classical nuclei.

All ring-polymer molecular dynamics (RPMD) and classical molecular dynamics (MD) trajectories are numerically integrated using the leap-frog integrator implemented in Gromacs-4.0.7. The simultaneous positions and velocities for each integration time step in the trajectories are stored for analysis. Unless otherwise stated, the RPMD equations of motion are integrated using a time step of 0.025 fs and classical MD trajectories are integrated using a time step of 1 fs. The classical MD trajectories are used only for the initial equilibration of the system and for additional results presented here in *SI Text*; all data presented in the main text are obtained using the quantized RPMD trajectories. Throughout the text, standard error estimates are calculated from five block-averages of the data.

From the initial geometry of the crystal structure, the system is equilibrated on the reactant potential energy surface V_{r} using classical MD. In a series of three equilibration steps, MD trajectories of length 10 ps in time are performed with progressively weaker harmonic restraints between the heavy atom positions and the crystal structure; the restraint force constants for the three equilibration runs are 100, 50, and 25 kcal mol^{-1} A^{-2}, respectively, and the runs are performed at constant volume and temperature using the Berendsen thermostat with a coupling constant of 0.01 ps (12). After initial equilibration to the reactants basin, the system is equilibrated on the full potential energy surface (Eq. **S1**) for an additional 100 ps of classical MD. Finally, the ring-polymer representation for the quantized hydride was introduced at the geometry of the relaxed classical system and equilibrated for an additional 1 ps using RPMD with the Berendsen thermostat.

Free Energy Sampling. The free energy (FE) profile in Fig. 1 of the main text is calculated as a function of the collective variable $\lambda(\mathbf{x}^{\mathrm{c}}) \equiv V_{\mathrm{r}}(\mathbf{x}^{\mathrm{c}}) - V_{\mathrm{p}}(\mathbf{x}^{\mathrm{c}})$, where $\mathbf{x}^{\mathrm{c}} \equiv (\mathbf{q}^{\mathrm{c}}, \mathbf{Q}_1, \ldots, \mathbf{Q}_N)$, and $\mathbf{q}^{\mathrm{c}} = \sum_{j=1}^{n} \mathbf{q}_j / n$ is the ring-polymer centroid of mass $m_{\mathrm{c}} = nm_n$. The umbrella sampling method (13) is used to efficiently sample this collective variable between the reactant and product basins. Independent RPMD sampling trajectories are performed using biasing potentials of the form

$$\sum_{j=1}^{n}[V_{\mathrm{EVB}}(\mathbf{x}^{(j)})] + \frac{1}{2}k_l(\lambda(\mathbf{x}^{\mathrm{c}}) - \lambda_l)^2, \qquad l = 1, \ldots, 20, \qquad \textbf{[S2]}$$

where the $\{k_l\}$ and $\{\lambda_l\}$ are listed in Table S1.

For the RPMD trajectories used to sample the FE profile, a ring-polymer bead mass of $m_n = 12/n$ amu was used to diminish the separation of timescales for the motion of the ring-polymer and the rest of the system. Changing this parameter does not affect the ensemble of configurations that are sampled in the calculation of the FE profile; it merely allows for the sampling trajectories to be performed with a larger simulation time step (0.1 fs) than is used in the dynamical trajectories. Furthermore, unlike the RPMD dynamical trajectories in which the long-range electrostatic contributions are updated every time step, we use twin-ranged cutoffs (4) in the FE sampling trajectories such that nonbonding interactions beyond 9 Å are only updated every 5 fs. Sampling trajectories are performed at constant temperature using the velocity rescaling thermostat (14) with a relaxation time of 0.05 ps.

The sampling trajectories are initialized in order of increasing λ_l, as follows. The first sampling trajectory ($l = 1$) was initialized from the equilibrated system in the reactant basin. After 25 ps of simulation, the configuration from this first sampling trajectory was used to initialize the second sampling trajectory ($l = 2$). After 25 ps of simulation, the configuration from the second trajectory was used to initialize the third sampling trajectory ($l = 3$), and so on. A total simulation length of 6 ns is sampled for each value of l, and the weighted histogram analysis method (WHAM) (15) is used to calculate the unbiased FE profile $F(\lambda)$ from the set of sampling trajectories.

To improve the overlap of the trajectories in coordinates other than $\lambda(\mathbf{x}^c)$, we follow the swapping procedure described by Warshel and coworkers (16). Configurations are swapped between neighboring values of windows every 100 ps, and the first 25 ps after a swap are discarded. Comparing results obtained with and without the use of this swapping protocol, we found no significant difference in the calculated free energy profile (Fig. S9). Each sampling trajectory for the calculation of the FE profile without swapping was also of length 6 ns in time.

In addition to calculating the quantized FE profile using the RPMD sampling trajectories, we repeat the sampling protocol with classical MD trajectories to obtain the classical FE profile for the intrinsic reaction. Fig. S2*A* compares these two results; the results for the quantized system are identical to those from Fig. 1*B* in the main text.

For the calculation of equilibrium ensemble averages, the configurations of the enzyme are aligned to remove overall translational and orientational diffusion. As in previous studies (1), this is done using the following iterative protocol. In a first step, all configurations in the ensemble are aligned to the crystal structure, and the atom positions of the aligned structure are averaged. In a second step, all of the configurations in the ensemble are aligned to the average structure from the first step. In all cases, the RMSD between the average structures of subsequent iterations converged to within 10^{-7} Å in less than 20 iterations.

The Dividing Surface Ensemble. Boltzmann-weighted sampling on the reaction dividing surface ($\lambda(\mathbf{x}^c) = -4.8$ kcal/mol) is performed with constrained molecular dynamics using the SHAKE algorithm (7). The existing implementation of SHAKE in Gromacs-4.0.7 is modified to constrain both classical MD and RPMD with respect to the collective variable $\lambda(\mathbf{x}^c)$. To remove the hard-constraint bias from the ensemble of configurations that is sampled in the constrained dynamics (17, 18), each sampled configuration is weighted by $[H(\mathbf{x}^c)]^{-1/2}$, where

$$H(\mathbf{x}^c) = (m_c)^{-1}|\nabla_{\mathbf{q}^c}\lambda(\mathbf{x}^c)|^2 + \sum_{k=1}^{N} M_k^{-1}|\nabla_{\mathbf{Q}_k}\lambda(\mathbf{x}^c)|^2. \qquad \textbf{[S3]}$$

Seven long, independent RPMD trajectories are run with the dividing surface constraint. These constrained trajectories are initialized from configurations obtained in the umbrella sampling trajectories that are restrained to the dividing surface region using Eq. **S2**, and they are performed at constant temperature using the velocity rescaling thermostat (14) with a relaxation time of 0.05 ps. Following an initial equilibration of 25 ps, each of the constrained trajectories is run for 1 ns, and dividing surface configurations are sampled every 4 ps. As with the umbrella sampling trajectories, the constrained dynamics utilize a ring-polymer bead mass of $m_n = 12/n$ amu to enable a time step of 0.1 fs.

To eliminate the effects of overall translational and rotational diffusion from the analysis of the reactive trajectories, the phase-space points for the reactive trajectories are aligned at $t = 0$ (i.e., the point of initial release from the dividing surface). This is done exactly as in the calculation of equilibrium averages. Using the ensemble of configurations corresponding to reactive trajectories at $t = 0$, the rotation and translation for each particular trajectory is determined. This translation and rotation is applied to the configuration of each time step in the trajectory, and only the rotation is applied to the velocities at each time step in the trajectory.

Calculation of the Transmission Coefficient. Using a dividing surface of $\lambda(\mathbf{x}^c) = \lambda^{\ddagger}$, the time-dependent transmission coefficient for the reaction is (19–22)

$$\kappa(t) = \frac{\langle \dot{\lambda}(\mathbf{x}^c(0),\dot{\mathbf{x}}^c(0))\theta(\lambda(\mathbf{x}^c(t)) - \lambda^{\ddagger})\rangle_{\lambda^{\ddagger}}}{\langle \dot{\lambda}(\mathbf{x}^c(0),\dot{\mathbf{x}}^c(0))\theta(\dot{\lambda}(\mathbf{x}^c(0),\dot{\mathbf{x}}^c(0)))\rangle_{\lambda^{\ddagger}}}, \qquad \textbf{[S4]}$$

where $\langle \ldots \rangle_{\lambda^{\ddagger}}$ denotes the Boltzmann-weighted distribution of configurations on the dividing surface, and $\theta(x)$ is the Heaviside function. The transmission coefficient is evaluated by initializing RPMD trajectories from configurations $(\mathbf{x}^c(0))$ on the dividing surface with velocities $(\dot{\mathbf{x}}^c(0))$ drawn from the Maxwell–Boltzmann distribution. These initial configurations are then correlated with the configurations $(\mathbf{x}^c(t))$ reached by the unconstrained RPMD trajectories after evolving the dynamics for time t.

In the current study, each sampled configuration on the dividing surface is used to generate three unconstrained RPMD trajectories that are evolved both forward and backward in time for 100 fs, such that 10,500 half-trajectories are released from the dividing surface. The initial velocities for each trajectory are drawn independently; these time-zero velocities, the time-zero positions, and the corresponding time-zero forces at the initial positions are used to initialize the leap-frog integrator.

In addition to calculating the transmission coefficient for the quantized hydride transfer using RPMD, we repeat the protocol with classical MD trajectories to obtain the classical transmission coefficient. Fig. S2*B* compares these two results; the results for the quantized system are identical to those from Fig. 1*C* in the main text.

Additional Measures of Dynamical Correlations. To confirm that Fig. 2 in the main text, which considers only heavy atom positions, did not neglect important dynamical correlations, we include the corresponding plots with all atoms for the enzyme included (Fig. S3). To examine the robustness of our conclusions about dynamical correlations in the system, we present various alternative measures of dynamical correlations in Figs. S4–S6. Fig. S4 presents alternative methods for analyzing the dynamical correlation measure $d_{ij}(t)$. In Fig. S5, we present a measure of dynamical correlations that are nonlocal in time,

$$d_{ij}^{\Delta t}(t) = \frac{\langle \mathbf{v}_i(t)\cdot\mathbf{v}_j(t+\Delta t)\rangle_t}{(\langle|\mathbf{v}_i(t)|^2\rangle_t\langle|\mathbf{v}_j(t+\Delta t)|^2\rangle_t)^{1/2}} - \frac{\langle \mathbf{v}_i(t)\cdot\mathbf{v}_j(t+\Delta t)\rangle}{(\langle|\mathbf{v}_i|^2\rangle\langle|\mathbf{v}_j|^2\rangle)^{1/2}}, \qquad \textbf{[S5]}$$

where $\langle \ldots \rangle_t$ and $\langle \ldots \rangle$ are defined as in the main text. In Fig. S6, we present a measure of dynamical correlations between perpendicular components of the velocity,

$$d_{ij}^{\perp,\xi_1,\xi_2}(t) = \frac{D_{ij}^{\perp,\xi_1,\xi_2}(t)}{(D_{ii}^{\perp,\xi_1,\xi_1}(t)D_{jj}^{\perp,\xi_2,\xi_2}(t))^{1/2}}, \qquad \textbf{[S6]}$$

where

$$D_{ij}^{\perp,\xi_1,\xi_2}(t) = \langle(\bar{v}_i^{\xi_1}(t) - \langle\bar{v}_i^{\xi_1}\rangle)(\bar{v}_j^{\xi_2}(t) - \langle\bar{v}_j^{\xi_2}\rangle)\rangle_t, \qquad \textbf{[S7]}$$

and where $\bar{\mathbf{v}}_i = (\bar{v}_i^1, \bar{v}_i^2, \bar{v}_i^3)$ is the absolute velocity vector in Cartesian coordinates. As for the measures presented in the main text, dynamical correlations are found to be localized in the substrate and cofactor regions, with only weak signatures in the protein residues surrounding the active site.

1. Agarwal PK, Billeter SR, Hammes-Schiffer S (2002) Nuclear quantum effects and enzyme dynamics in dihydrofolate reductase catalysis. *J Phys Chem B* 106:3283–3293.
2. Warshel A, Weiss RM (1980) An empirical valence bond approach for comparing reactions in solutions and in enzymes. *J Am Chem Soc* 102:6218–6226.
3. Fierke CA, Johnson KA, Benkovic SJ (1987) Construction and evaluation of the kinetic scheme associated with dihydrofolate-reductase from *Escherichia coli*. *Biochemistry* 26:4085–4092.
4. van Gunsteren WF, et al. (1996)*Biomolecular Simulation: The GROMOS96 Manual and User Guide* (Hochschuleverlag AG an der ETH Zürich, Zürich, Switzerland).
5. Wong KF, Watney JB, Hammes-Schiffer S (2004) Analysis of electrostatics and correlated motions for hydride transfer in dihydrofolate reductase. *J Phys Chem B* 108:12231–12241.
6. Darden T, York D, Pedersen L (1993) Particle mesh Ewald: An N·log(N) method for Ewald sums in large systems *J Chem Phys* 98:10089–10092.
7. Ryckaert JP, Ciccotti G, Berendsen HJC (1977) Numerical-integration of cartesian equations of motion of a system with constraints: Molecular-dynamics of *n*-alkanes. *J Comput Phys* 23:327–341.
8. Sawaya MR, Kraut J (1997) Loop and subdomain movements in the mechanism of *Escherichia coli* dihydrofolate reductase: Crystallographic evidence. *Biochemistry* 36:586–603.
9. Arora K, Brooks CL (2009) Functionally important conformations of the Met20 loop in dihydrofolate reductase are populated by rapid thermal fluctuations. *J Am Chem Soc* 131:5642–5647.
10. Khavrutskii IV, Price DJ, Lee J, Brooks CL (2007) Conformational change of the methionine 20 loop of *Escherichia coli* dihydrofolate reductase modulates pK_a of the bound dihydrofolate. *Protein Sci* 16:1087–1100.
11. Berendsen HJC, Grigera JR, Straatsma TP (1987) The missing term in effective pair potentials. *J Phys Chem* 91:6269–6271.
12. Berendsen HJC, Postma JPM, Vangunsteren WF, Dinola A, Haak JR (1984) Molecular-dynamics with coupling to an external bath. *J Chem Phys* 81:3684–3690.
13. Torrie GM, Valleau JP (1977) Nonphysical sampling distributions in Monte Carlo free-energy estimation: Umbrella sampling. *J Comput Phys* 23:187–199.
14. Bussi G, Donadio D, Parrinello M (2007) Canonical sampling through velocity rescaling. *J Chem Phys* 126:014101.
15. Kumar S, Bouzida D, Swendsen RH, Kollman PA, Rosenberg JM (1992) The weighted histogram analysis method for free-energy calculations on biomolecules. I. The method. *J Comput Chem* 13:1011–1021.
16. Liu HB, Warshel A (2007) Origin of the temperature dependence of isotope effects in enzymatic reactions: The case of dihydrofolate reductase. *J Phys Chem B* 111:7852–7861.
17. Zichi DA, Ciccotti G, Hynes JT, Ferrario M (1989) Molecular-dynamics simulation of electron-transfer reactions in solution. *J Phys Chem* 93:6261–6265.
18. Frenkel D, Smit B (2002) *Understanding Molecular Simulation: From Algorithms to Applications*, Computational Science Series (Academic, San Diego), 2nd Ed.
19. Bennett CH (1977) *Algorithms for Chemical Computations*, ACS Symposium Series (American Chemical Society, Washington, DC) Vol. 46, pp 63–97.
20. Chandler D (1978) Statistical-mechanics of isomerization dynamics in liquids and transition-state approximation. *J Chem Phys* 68:2959–2970.
21. Craig IR, Manolopoulos DE (2005) A refined ring polymer molecular dynamics theory of chemical reaction rates. *J Chem Phys* 123:034102.
22. Craig IR, Manolopoulos DE (2005) Chemical reaction rates from ring-polymer molecular dynamics. *J Chem Phys* 122:084106.

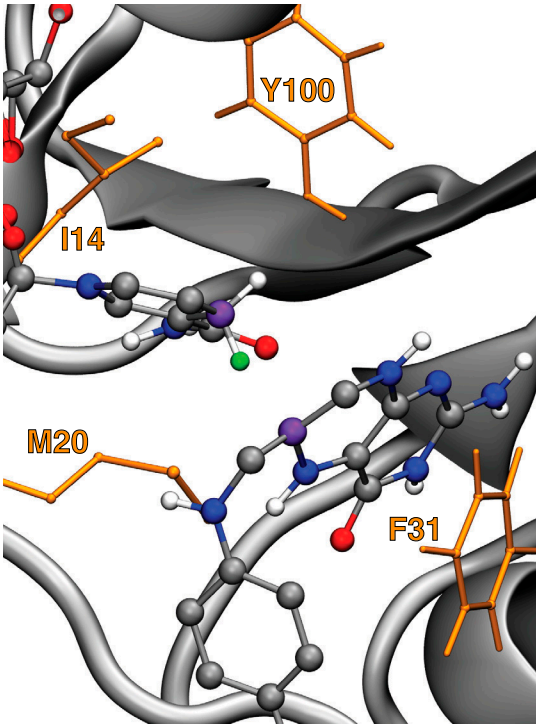

Fig. S1. The active site region of the DHFR enzyme, with the transferring hydride (green) in the reactant state, the donor and acceptor carbon atoms in purple, and relevant protein residues in gold.

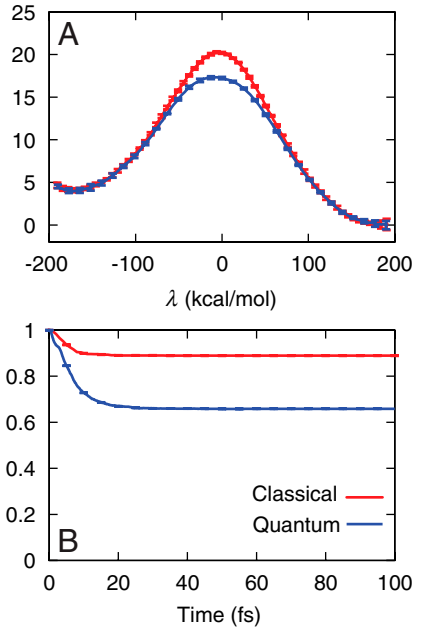

Fig. S2. (*A*) The quantized and classical free energy profiles for the reaction. (*B*) The quantized and classical time-dependent transmission coefficient corresponding to the dividing surface at $\lambda(\mathbf{x}) = -4.8$ kcal/mol.

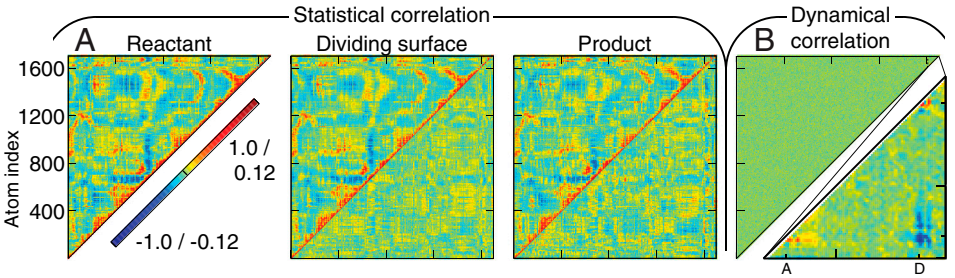

Fig. S3. (*A*) (Upper triangles) The covariance c_{ij} among position fluctuations in DHFR, plotted for the reactant, dividing surface, and product regions. All atoms are indexed according to PDB ID code 1RX2. (Lower triangles) The difference with respect to the plot for the reactant basin. (*B*) (Upper triangle) The integrated dynamical correlation measure d_{ij}, indexed as in (*A*). (Lower triangle) The substrate and cofactor regions are enlarged. Dynamical correlations between atom-pairs that share a holonomic constraint are excluded from part B. Comparison of the current figure (which includes all atoms) with Fig. 2 in the main text (which includes only heavy atoms) leaves the conclusions from the main text unchanged.

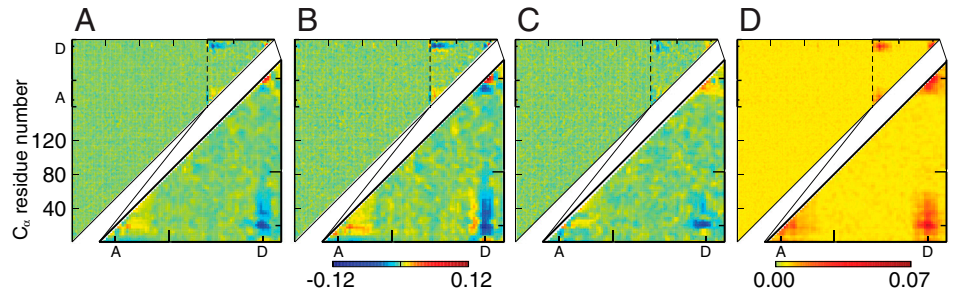

Fig. S4. Alternative measures of the dynamical correlation. (*A*) The integrated dynamical correlation measure $d_{ij} = \int_{-\tau}^{\tau} dt d_{ij}(t)$, reproduced from Fig. 2*E* of the main text. (*B*) Including only the forward-integrated time, $\int_{0}^{\tau} dt d_{ij}(t)$. (*C*) Including only the backward-integrated time, $d_{ij} = \int_{-\tau}^{0} dt d_{ij}(t)$. (*D*) Including the integrated absolute value, $\int_{-\tau}^{\tau} dt |d_{ij}(t)|$. In all cases, $\tau = 100$ fs.

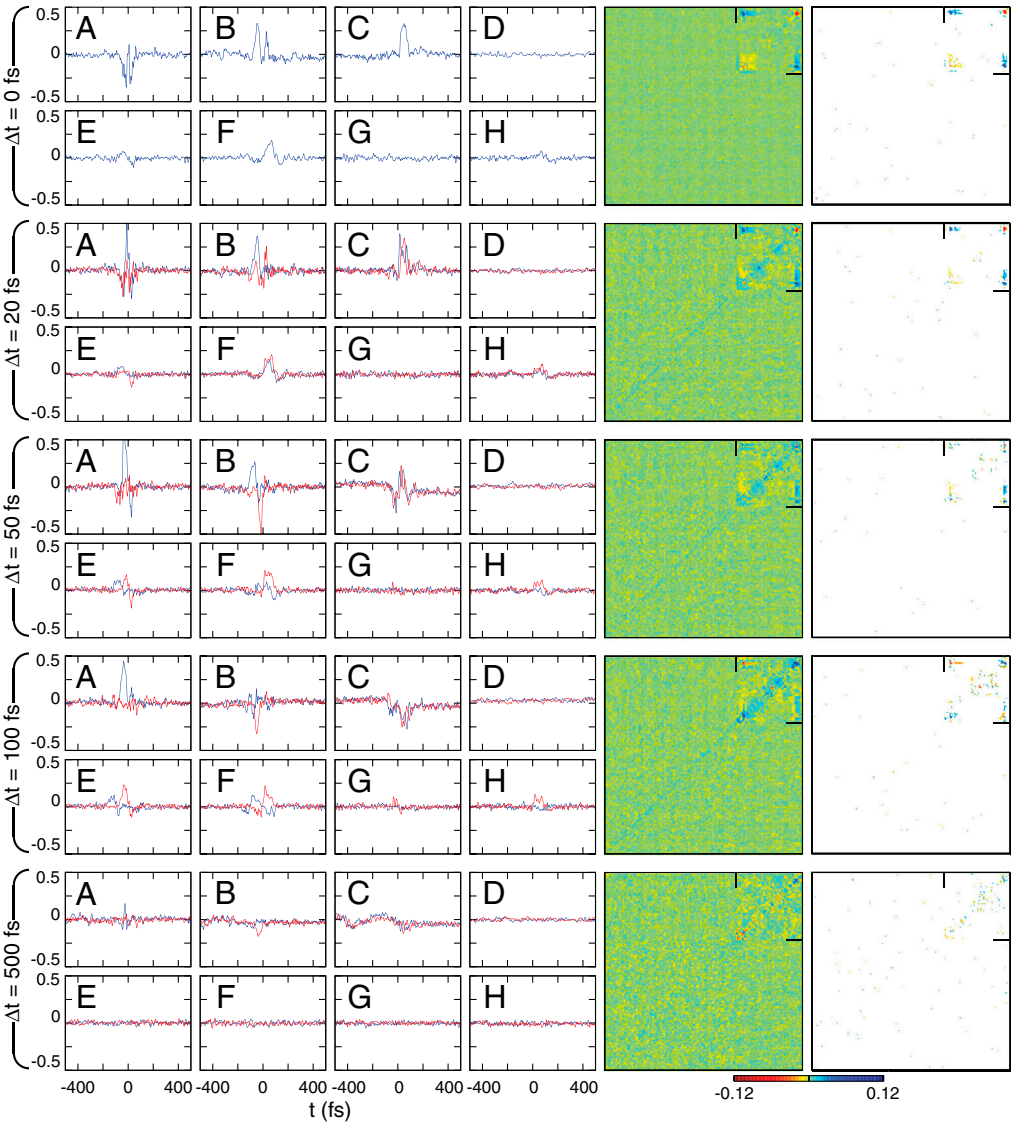

Fig. S5. (*A–H*) The measure of temporally nonlocal dynamical correlations, $d_{ij}^{\Delta t}(t)$, plotted at various separation times Δt and for various atom pairs, including (*A*) the donor and acceptor atom pair, (*B*) the substrate-based C_7 and the acceptor atom pair, (*C*) the cofactor-based CN_4 and donor atom pair, (*D*) the active site-based protein atoms that define the distance Θ_2 in Fig. 4*B* (*E*) the active-site-based backbone I4 O and the acceptor atom pair, (*F*) the active-site-based backbone I4 O and the donor atom pair, (*G*) the active-site-based backbone G95 C_α and the acceptor atom pair, and (*H*) the active-site-based backbone G95 C_α and the donor atom pair. Two curves (red and blue) are plotted, because $d_{ij}^{\Delta t}(t)$ is not symmetric with respect to atom indices *i* and *j* for nonzero Δt. At right, the integrated measure $d_{ij}^{\Delta t} = \int_{-\tau}^{\tau} dt d_{ij}^{\Delta t}(t)$ for each lag time, plotted as a function of the protein α-carbon atoms and the heavy atoms of the substrate and cofactor, as in Fig. 2*E* in the main text. In all cases, $\tau = 100$ fs. At far right, the same integrated measure is replotted, only displaying data points for which the magnitude of the integrated measure exceeds twice the estimated standard error.

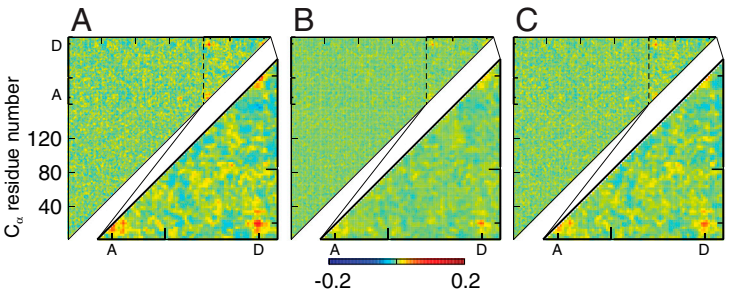

Fig. S6. The measure of dynamical correlations between perpendicular components of the velocity, $d_{ij}^{\perp,\xi_1,\xi_2}(t)$. (*A*) The integrated measure $d_{ij}^{\perp} = \sum_{\xi_1,\xi_2=1}^{3} \int_{-\tau}^{\tau} dt d_{ij}^{\perp,\xi_1,\xi_2}(t)$ that includes all components. (*B*) The integrated measure $d_{ij}^{\perp} = \sum_{\xi}^{3} \int_{-\tau}^{\tau} dt d_{ij}^{\perp,\xi,\xi}(t)$ that includes only diagonal components. (*C*) The integrated measure $d_{ij}^{\perp} = \sum_{\xi_1 \neq \xi_2=1}^{3} \int_{-\tau}^{\tau} dt d_{ij}^{\perp,\xi_1,\xi_2}(t)$ that includes only off-diagonal components. In all cases, $\tau = 100$ fs, and the integrated measures are plotted as a function of the protein α-carbon atoms and the heavy atoms of the substrate and cofactor, as in Fig. 2*E* in the main text.

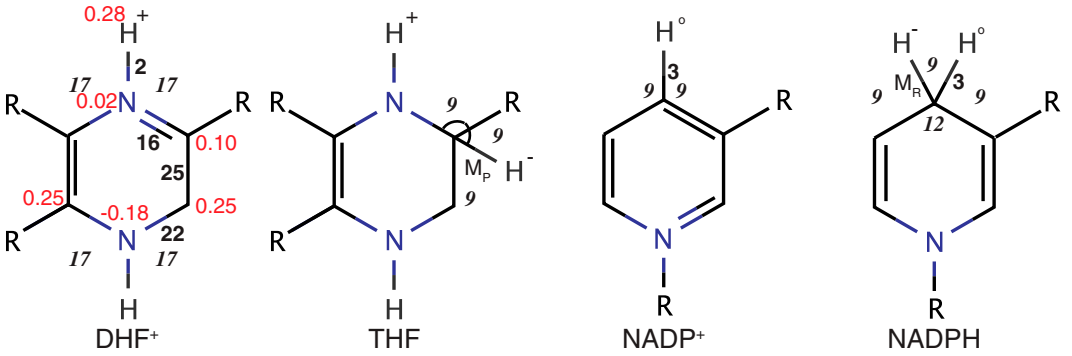

Fig. S7. Modifications to the GROMOS 43A1 united atom forcefield only involve the DHF^+, THF, $NADP^+$, and NADPH species. The resulting potential energy surface is as close as possible to that used in earlier studies of statistical correlation in DHFR hydride transfer catalysis (1). Only parameters that differ from the GROMOS forcefield are indicated; parameters shown for DHF^+ differ with respect to those for 7,8-dihydrofolate (DHF). In red, the atomic charges for DHF^+ are shown. In black, the bond-type (bold) and angle-type (italics) indices for the GROMOS forcefield are shown. Explicit representations are used for the transferring hydride (H^-) in the THF and NADPH species, the pro-*S* hydrogen atom (H°) in the NADPH and $NADP^+$ species, and the proton (H^+) attached to the nearest neighbor of the donor carbon. Firstly, we describe the treatment of H^-. The transferring hydride interacts with the donor and acceptor carbons via Morse potentials M_R and M_P, respectively (1). Following GROMOS convention, nonbonding interactions are excluded between H^- and its first-, second-, and third-nearest neighbors, defined in terms of bonding connectivity. Additionally, nonbonding interactions between H^- and the H°, donor, and acceptor atoms are excluded, regardless of the local bonding environment of the H^- atom. Secondly, we describe the treatment of H°. The bond length for H° is constrained to a fixed value of 1.09 Å , and planarity of H° with respect to the nicotinamide ring in $NADP^+$ is enforced using the planar improper dihedral angle potential in GROMOS. As for the hydride, nonbonding interactions are excluded between H° and its first-, second-, and third-nearest neighbors. Thirdly, we describe the treatment of H^+. Nonbonding interactions are excluded between H^+ and its first- and second-nearest neighbors; third-nearest neighbor nonbonding interactions are treated through using a 1–4 potential. For the LJ interactions involving these explicit hydrogen atoms, H^+ is treated using the parameters for a charged hydrogen, and both H° and H^- are treated using the parameters for a hydrogen bound to a carbon. For the LJ interactions involving the donor and acceptor, these atoms are treated using the parameters for a bare carbon atom.

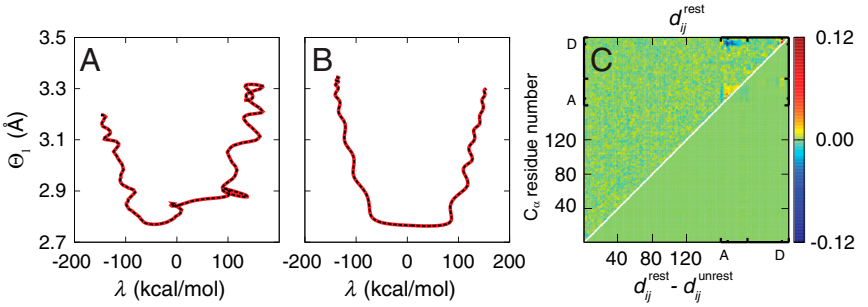

Fig. S8. Tests of the degree to which the weak harmonic restraints impact the dynamics of the reactive trajectories. (*A*) Comparison of two trajectories that are initialized from the same positions and velocities on the dividing surface, which are calculated with (red) and without (black) the weak restraints. Trajectories are evolved for a total of 200 fs and are viewed in the plane of the donor-acceptor distance ($\Theta_1(\mathbf{x}^c)$) and the reaction progress variable ($\lambda(\mathbf{x}^c)$). (*B*) In red, the mean pathway from the ensemble of 750 reactive trajectories, $\sigma = (\langle\lambda(\mathbf{x}^c)\rangle_t, \langle\Theta_1(\mathbf{x}^c)\rangle_t)$, calculated for trajectories obtained with the weak restraints. In black, the mean pathway from the ensemble of 750 trajectories that are initialized from the same phase-space points but which do not include the weak restraints. (*C*) (Upper triangle) The dynamical correlation measure d_{ij}^{rest}, calculated from an ensemble of 750 reactive trajectories using the weak harmonic restraints; this quantity is identical to the that reported in Fig. 2*E* of the main text, except that fewer trajectories are used here. (Lower triangle) The difference between d_{ij}^{rest} and d_{ij}^{unrest}, which is calculated from the ensemble of 750 trajectories that are initialized from the same phase-space points but which do not include the weak restraints. For all three tests, the impact of the weak restraints on the dynamics of the reactive trajectories is undetectable.

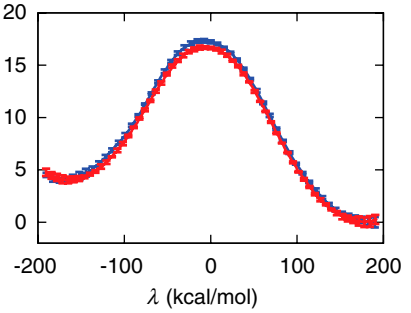

Fig. S9. Free energy profiles obtained with (red) and without (blue) swapping of configurations from neighboring 6 ns sampling trajectories in the WHAM calculation.

Table S1. The umbrella sampling parameters $\{\lambda_I\}$ and $\{k_I\}$ in units of kcal/mol and mol/kcal, respectively

I	λ_I	k_I
1	−188.7	0.002
2	−154.0	0.002
3	−120.0	0.002
4	−87.1	0.002
5	−57.4	0.004
6	−56.1	0.002
7	−35.8	0.004
8	−18.3	0.004
9	−17.8	0.008
10	−6.4	0.008
11	1.4	0.004
12	1.5	0.008
13	4.3	0.006
14	14.2	0.004
15	23.3	0.002
16	34.2	0.004
17	57.9	0.002
18	95.8	0.002
19	135.7	0.002
20	170.0	0.000